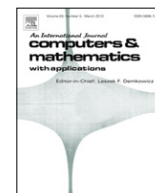




Contents lists available at SciVerse ScienceDirect

Computers and Mathematics with Applications

journal homepage: www.elsevier.com/locate/camwa

Tracking control of a biaxial piezo-actuated positioning stage using generalized Duhem model

Chih-Jer Lin*, Po-Ting Lin

Graduate Institute of Automation Technology, National Taipei University of Technology, Taipei 10608, Taiwan

ARTICLE INFO

Keywords:

Hysteresis
Piezo-actuator
Duhem model
Dahl model
Bouc–Wen model
Particle swarm optimization

ABSTRACT

Nonlinear hysteresis modeling is studied using a novel PZT-actuated flexure-based mechanism. To compare the performance of variant hysteresis models with respect to the tracking reference, we reformulate the Bouc–Wen model, the Dahl model and the Duhem model as a generalized Duhem model. System parameters for these three hysteresis models are formulated into nonlinear optimization problems with constraints. These optimization problems are solved by the particle swarm optimization method. Since the Duhem model includes both electrical and mechanical domains, it has a smaller modeling error compared to the other two hysteresis models. The simulation results are confirmed by modeling the proposed biaxial piezo-actuated positioning stage of these hysteresis models. Cross-coupling effects between the X- and Y-axis actuation are also alleviated by a novel feedforward compensation mechanism based on the Duhem model with crossover terms. Finally, a real-time experiment is performed to confirm the feasibility of the proposed method. The experimental results validate the capability of the proposed controller to achieve precision tracking tasks with submicron precision.

© 2011 Elsevier Ltd. All rights reserved.

1. Introduction

In recent years, the demand for ultra-precision positioning systems has increased in the micro/nano semiconductor and ultra-precision machining industries. To meet the requirements of precise motion at sub-micro/nano scale and high speed, high accuracy and large load, piezoelectric actuators (PAs) are essential drive positioning mechanisms for achieving ultra-precision. The word “piezoelectricity”, which is derived from the Greek word “piezo” for pressure, refers to the “pressure electricity” discovered by Pierre and Jacques Curie in 1880. The Curie brothers demonstrated the so-called *direct piezoelectric effect*, which is the generation of an electric charge in response to applied pressure or stress. For precision positioning purpose, the *converse piezo effect* is usually applied to produce precise displacements in response to the applied electric field. The advantages of PA are its light weight, small size, high electrical–mechanical coupling efficiency, broadband drive capabilities, and very high set-point accuracy (i.e., to within 1–10 nm). Therefore, PAs are highly effective actuators for flexure-based mechanisms. However, due to the non-centrosymmetric nature of piezoelectric materials, a converse piezo effect produces hysteresis and constitutive nonlinearities at all drive levels. The hysteresis effect between the displacement and the electric field often decreases positioning precision. Additionally, the effect is not differentiable and conducive to one-to-one nonlinear mapping. Its nonlinearity with local memory causes positioning errors and critically limits the operating speed and precision of PA.

Nonlinear hysteresis effects can be corrected by incorporating charge current control or model-based control. However, the charge current control may not only cause drift and saturation problems, it can also substantially reduce operating

* Corresponding author. Fax: +886 2 27712171.

E-mail address: cjlin@ntut.edu.tw (C.-J. Lin).

range. Another solution is to model the converse piezo effect so that feed-forward compensation can be used correct hysteresis nonlinearity based on the inverse-hysteresis model. Mathematical models of hysteresis behavior proposed in the literature include the Preisach model [1], the generalized Maxwell-slip hysteretic model [2], Prandtl–Ishlinskii model [3], Duhem model [4], Bouc–Wen model [5–7], Dahl model [8], Chua–Stromsmoe model [9] and Jiles–Atherton model [10]. The Preisach model is among the most popular hysteresis models because it captures a large class of hysteresis maps with complex reversal behavior by using an integral model with an infinite number of hysteretic operators. However, the Preisach model requires substantial computing resources to perform the simulations needed to establish the grids of the plane. Two other integral hysteresis models, the generalized Maxwell-slip model and the Prandtl–Ishlinskii model, use different kernel functions.

In contrast with the integral models discussed above, a mass-spring has been suggested for use in approximating a hysteron model [1]. An alternative model in the class of hysteresis models studied in [4] is the Duhem model, which describes the relation between the magnetic field strength $H(t)$ and the magnetic flux density $B(t)$ of a ferromagnetic material as.

$$\dot{B}(t) = a |\dot{H}(t)| \cdot [bH(t) - B(t)] + c\dot{H}(t). \quad (1)$$

Although the Duhem model was originally developed to describe magnetic hysteresis, it has proven suitable for describing piezo-electric hysteresis [11]. Variations of the Duhem model proposed in various contexts include the Dahl friction model and the Bouc–Wen model, which was originally proposed by Bouc in 1967 and later generalized by Wen in 1976 to describe the typical hysteresis [5]. The Bouc–Wen model is described by the following first-order nonlinear differential equation:

$$\dot{h}(t) = \alpha \dot{V} - \beta |\dot{V}(t)| \cdot h(t) \cdot |h(t)|^{n-1} - \gamma \dot{V} |h(t)|^n, \quad (2)$$

where $h(t)$ represents the hysteretic state variable and $V(t)$ is the input voltage; parameters α , β , γ control the amplitudes and shapes of the hysteresis loop, and n controls the smoothness of transition from an elastic response to a plastic response. Zhang et al. [12] used the genetic algorithm (GA) for setting hysteresis parameters in the Bouc–Wen model and performed numerical simulations to confirm the feasibility of the identification method. However, their experimental data are difficult to verify because the selected fitness function includes a term for differentiating acceleration. The solution proposed by Ha et al. [6] is identify the hysteresis model parameters and the PA simultaneously according to three fitness functions; however, feed-forward control was not proposed and discussed. Jang et al. [13] discussed a piezoelectric actuator-driven system with asymmetric hysteresis and established a feed-forward controller based on the proposed asymmetric hysteresis model. Lin and Chen [7] used evolutionary algorithms to optimize parameters of the Bouc–Wen model of PEA hysteresis and proposed the real-time architecture. Although the Dahl model is widely used in friction modeling, it has limited effectiveness for piezoelectric hysteresis modeling. The second-order Dahl model proposed in Ref. [8] reduces the number of parameters required by the nonlinear hysteretic system to describe the inverse Dahl model and simplifies the calculation of feed-forward compensation. Another recent advance is the novel control scheme with inverse Dahl model augmented with repetitive proportional-integral-derivative (PID) proposed by Xu and Li. They showed that the Dahl model is better than the Bouc–Wen model for describing nonsymmetrical hysteresis given an equal number of model parameters [8]. The second-order Dahl model with state space representation describes piezoelectric hysteresis force as

$$F_h = C_h V \quad (3)$$

$$\dot{V}(t) = A_h V \cdot \dot{x} + B_h u_p \cdot \dot{x}, \quad (4)$$

where variable x denotes the x -axis displacement, $V = [q_1 q_2]^T$ is state vector for the second-order model, $u_p = 30$ is the constant recommended in Ref. [8], and A_h , B_h , C_h are as follows.

$$A_h = \begin{bmatrix} 0 & 1 \\ -a_2 & -\text{sgn}(\dot{x})a_1 \end{bmatrix}, \quad B_h = \begin{bmatrix} 0 \\ 1 \end{bmatrix}, \quad C_h = [b_1 \quad \text{sgn}(\dot{x})b_0]. \quad (5)$$

The experimental results in this study show that, because the tracking reference is a sinusoidal signal, the second-order Dahl model describes the hysteresis better than the Bouc–Wen model does. However, when the tracking reference for modeling is a triangle signal, the Bouc–Wen model of hysteresis is better. The Duhem model, however, is robust with either the sinusoidal signal or the triangle signal. Therefore, the robustness of the hysteresis model is an essential consideration when comparing tracking references. Below, the robustness of the hysteresis models is analyzed for different input responses.

A flexure is a frictionless device based on the elastic deformation of a solid material. Since it requires no lubricants or consumables, it is suitable for vacuum operation. Flexure-based mechanisms (FBMs) are piezoelectric actuator applications with functions controlled by static properties. For many years, researchers have used elastic mechanisms for micro-positioning and micromanipulation in the scanning tubes and specimen stages of scanning electron microscopes (SEMs), for positioning the probe in atomic force microscopes (AFMs) [14], for various operations in cell microsurgery, and for precision measurement and alignment of wafers in deep ultraviolet lithography and scanning probe microscopy (SPM) [15]. An FBM is usually driven directly by a PA, and another scanning device uses a mechanical amplifier to extend or reverse

the motion produced by the PA; many displacement-amplifying mechanisms have been proposed to support multi-axis precision positioning for sub-micron wafer alignment. Ryu et al. [16] optimized the design of a hinge-based frame-leveraged mechanical amplifier for performing X–Y positioning during wafer alignment. Chang et al. [17] developed a novel three degree-of-freedom micropositioner for deep ultraviolet lithography applications. A flexure-guided piezo-actuated scanning stage with 50 μm range and sub-nanometer resolution has also been investigated [18]. Both direct drive serial-kinematic [19] and parallel-kinematic [20] positioning stages using FBM have been developed for high-speed purposes. For wafer alignment tasks, the biaxial piezo-actuated XY-positioning stage is usually used to perform positioning tasks. However, positioning precision is degraded by the cross coupling effect resulting from simultaneous actuation of the X- and Y-PAs [21]. To improve the tracking performance of biaxial tracking tasks, this study proposes a hysteresis model with crossover term to alleviate the cross coupling effect between X- and Y-stages during precision tracking tasks.

The literature inspired the proposed generalized Duhem model (GDM) for the hysteresis model of a piezo-electrical actuator. The Duhem model, Bouc–Wen model and Dahl model are formulated as the specified GDM for modeling the piezo-actuated stage. As reported in Ref. [22], the responses of the various hysteresis models depend on the tracking references. Therefore, this study compares the robustness of these three hysteresis models in terms of their tracking references. To achieve precise positioning without cross-coupling effects, the design of a model-based feed-forward controller must compensate for both hysteresis nonlinearity and cross-coupling effects. First, the inverse-hysteresis model based on Duhem model, Bouc–Wen models and Dahl model are studied to estimate the hysteresis dynamics in this study. The robustness of the hysteresis models based on these three models is then discussed in terms of tracking references. However, since identifying hysteresis parameters and FBM determines the feasibility of feed-forward control, particle swarm optimization (PSO) is used to identify the system parameters. The Duhem and Bouc–Wen models with crossover terms are also used to alleviate cross-coupling effects between the X and Y stage. To verify its feasibility and effectiveness, a feed-forward control based on the proposed method is implemented using a real-time DSP controller. The rest of this paper is organized as follows. Section 2 presents a generalized Duhem model (GDM) for the hysteresis model of the piezo-electrical actuator, where Duhem model, Bouc–Wen model and Dahl model are formulated as the specified GDM for modeling the piezo-actuated stage. Section 3 introduces the design of biaxial piezo-actuated positioning stage and the experimental setup, in which the range of motion is approximately $10\ \mu\text{m} \times 10\ \mu\text{m}$. System parameters are identified according to PSO. The performance of various hysteresis models are then compared in terms of the tracking reference. Section 4 presents the Duhem model with crossover terms for alleviating cross-coupling effects between the X and Y stage. Real-time experiments are then performed to confirm the feasibility of the implementation. Finally, conclusions are drawn in Section 5.

2. System description and generalized Duhem hysteresis modeling

The proposed compact micropositioner design based on monolithic mechanism was implemented to provide translation in the X- and Y-directions. Fig. 1 shows the design concept of a nested XY piezo micro mechanism, where the X-axis positioning mechanism includes the Y-axis positioning mechanism. The FBM is actuated by two PAs, and this monolithic mechanism enables independent motion of the translation platform in the X and Y directions. An electrical voltage applied to the PA of the X- or Y-axis increases the length and applies a pushing force to the X- or Y-moving stages, respectively. In this case, the micro stage has two degrees of freedom, and the axes are connected in series. Displacement of the moving stage causes a strain on the plane springs when the PAs are actuated.

2.1. Modeling of the piezo-actuated flexure-based stage

If the X-stage and Y-stage are not actuated simultaneously, and if each stage works in the standalone mode, the cross-coupling effect between the X- and Y-axis is negligible. To simplify the complexity of the mechanism, the structure was modeled in terms of the lump mass discrete system (Fig. 2). Each PA-actuated FBM stage can be modeled as follows [7].

$$m\ddot{x} + b\dot{x} + kx = k(d_e u - h), \quad (6)$$

where m is the equivalent mass, b is the equivalent damping, k is the equivalent stiffness, x is the output displacement, and d_e is the piezoelectric coefficient. The $h(t)$ represents the hysteretic state variable, and $u(t)$ is the input voltage; h represents the nonlinear hysteretic term, which is nonlinear with respect to the applied voltage. Hysteresis phenomena in the PEA result in a nonlinear rather than linear relation between the actuated force and the applied voltage. The proposed solution is to describe the hysteresis for feed-forward compensation with a nonlinear model. The generalized Duhem model for describing nonlinear hysteresis is studied and discussed below.

2.2. Generalized Duhem model for the PA FBM with hysteresis nonlinearity

The underlying concept of using the *generalized Duhem model* (GDM) to formulate hysteresis models that are either independent or dependent on rate was first presented in [22]. Although Oh and Bernstein derived semi-linear models for rate-independent and rate-dependent generalized Duhem models, their focus was on the hysteretic nonlinearities of

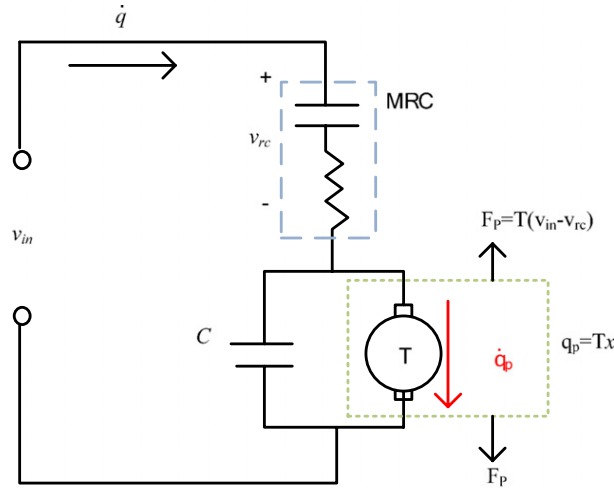


Fig. 1. Model of a piezoelectric actuator using Duhem model.

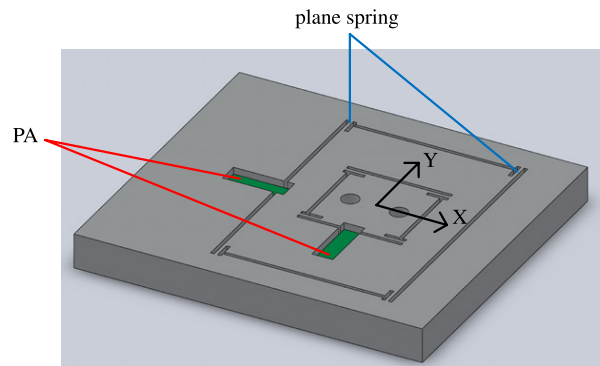


Fig. 2. The dimensional model of PA actuated XY stage.

backlash, bifurcation, and buckling. This study therefore reformulates the Bouc–Wen model, Dahl model and Duhem model as GDMs. Consider the following single-input single-out GDM for the piezo-electrical hysteresis.

$$\dot{x}(t) = f(x(t), u(t)) \cdot g(\dot{u}(t)), \quad x(0) = x_0, \quad t \geq 0 \quad (7)$$

$$y(t) = h(x(t), u(t)), \quad (8)$$

where $x : [0, \infty) \rightarrow R^n$ is a continuous internal state vector, $u : [0, \infty) \rightarrow R^n$ is the input voltage, which is continuous and piecewise C^1 , $f : R^n \times R \rightarrow R^{n \times r}$ is continuous, $g : R \rightarrow R^r$ is continuous and satisfies $g(0) = 0$, $y : [0, \infty) \rightarrow R^n$, and $h : R^n \times R \rightarrow R$. A solution to (8) is assumed to exist and to be unique on all finite intervals. The output $y(t)$ of the hysteresis model is continuous and piecewise C^1 .

2.2.1. Bouc–Wen model reformulated as GDM

Fig. 3 is a schematic diagram of FBM using PA; its dynamic equation is

$$m\ddot{x} + b\dot{x} + kx = k(d_e u - h), \quad (9)$$

where $h(t)$ represents the hysteretic state variable and $u(t)$ is the input voltage; parameters α , β , γ control the amplitudes and shapes of the hysteresis loop, and n controls the transition from elastic to plastic response as follows.

$$\dot{h}(t) = \alpha \dot{u} - \beta |\dot{u}(t)| \cdot h(t) \cdot |h(t)|^{n-1} - \gamma \dot{u} |h(t)|^n \quad (10)$$

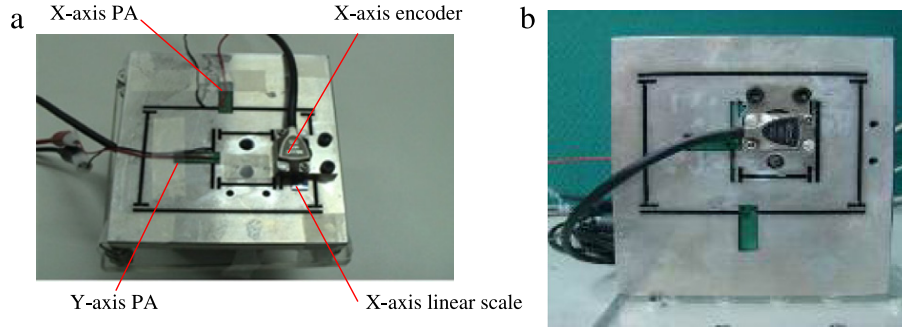


Fig. 3. (a) The top-view of the PA-actuated XY stage and (b) the bottom-view of the PA-actuated XY stage.

where the piezoelectric hysteresis force is defined as $F_h = k \cdot h$,

$$\begin{aligned} \dot{F}_h(t) &= \begin{bmatrix} \frac{\alpha}{k} - \frac{\beta}{k} h |h|^{n-1} - \frac{\gamma}{k} |h|^n \\ \frac{\alpha}{k} + \frac{\beta}{k} h |h|^{n-1} - \frac{\gamma}{k} |h|^n \end{bmatrix}^T \cdot \begin{bmatrix} \dot{u}_+ \\ \dot{u}_- \end{bmatrix} \\ &= f(F_h(t)) \cdot g(\dot{u}(t)) \end{aligned} \quad (11)$$

$$y(t) = x(t) = h(F_h(t), u(t)), \quad (12)$$

where $\dot{u}_+ \triangleq \max\{0, \dot{u}(t)\}$, $\dot{u}_- \triangleq \min\{0, \dot{u}(t)\}$. Comparison with the definition in Eq. (7) shows that Bouc–Wen model is a special case of GDM in which $\dot{F}_h(t)$ depends only on $\dot{u}(t)$ but it is independent of $x(t)$.

2.2.2. Dahl model reformulated as GDM type

Consider the schematic diagram of FBM using PA. Its dynamic equation is

$$m\ddot{x} + b\dot{x} + kx = F_d - F_h = T_{em} \cdot u(t) - C_h \cdot V, \quad (13)$$

where T_{em} is the electromechanical transformer ratio, which is equal to $k \cdot d_e$ of Eq. (9). The F_d describes the actuated force from the PA, and $F_h = C_h V$ is piezoelectric hysteresis force, where $V = [q_1 \ q_2]^T$ is the state vector for the second-order model. The second-order Dahl model with state space representation, as reported in Ref. [23], is modified as

$$\dot{V}(t) = A_h V \cdot \dot{x} + B_h u_p \cdot \dot{x}, \quad (14)$$

where the variable x denotes the x -axis displacement and $u_p = 30$ is the constant recommended in Ref. [18]. Differentiating Eq. (13) with respect to t and substituting $\dot{V}(t)$ gives

$$\begin{aligned} \dot{F}_h(t) &= C_h \cdot \dot{V} = C_h \cdot (A_h \cdot V \cdot \dot{x} + B_h \cdot u_p \cdot \dot{x}) \\ &= \begin{bmatrix} -a_2 b_0 \operatorname{sgn}(\dot{x}) & b_1 - a_1 b_0 \end{bmatrix} \cdot V \dot{x} + \operatorname{sgn}(\dot{x}) \cdot b_0 \cdot u_p \dot{x} \\ &= (-a_2 b_0 \cdot q_1 + b_0 u_p) \operatorname{sgn}(\dot{x}) \dot{x} + (b_1 - a_1 b_0) \cdot q_2 \dot{x} \\ &= \begin{bmatrix} -a_2 b_0 \cdot q_1 + b_0 u_p + (b_1 - a_1 b_0) \cdot q_2 \\ a_2 b_0 \cdot q_1 - b_0 u_p + (b_1 - a_1 b_0) \cdot q_2 \end{bmatrix}^T \cdot \begin{bmatrix} \dot{x}_+ \\ \dot{x}_- \end{bmatrix} \\ &= f(F_h(t)) \cdot g(\dot{x}(t)), \end{aligned} \quad (15)$$

where $\dot{x}_+ \triangleq \max\{0, \dot{x}(t)\}$, $\dot{x}_- \triangleq \min\{0, \dot{x}(t)\}$. Comparison with the definition in Eq. (7) shows that the Dahl model is a special case of GDM. Although the $\dot{F}_h(t)$ depends on $\dot{x}(t)$, the hysteresis force of Dahl model is independent of $\dot{u}(t)$.

2.2.3. Duhem model reformulated as GDM type

In 1997, Goldfarb and Celanovic [24] proposed a PA model based entirely on physical principles. Their model includes both electric and mechanical domains as well as the connection between the two domains. It also describes both hysteresis nonlinearity and linear dynamics. Adriaens et al. [25] considered how voltage steering is related to charge steering when using piezoelectric materials as actuators. They also proposed the Duhem model, which is an improvement on the hysteresis and dynamical model developed in [25]. Fig. 9 shows the PA model. The generalized Maxwell resistive capacitance, which is represented by the MRC element, relates the electrical voltage of the element to the charge. For example, the capacitive element is charged as displacement occurs on the mechanical side. Eq. (19) describes the electromechanical interactions

between the electrical port and the mechanical port in this PA model. The complete set of electromechanical equations is as follows:

$$m\ddot{x} + b\dot{x} + kx = F_t = T \cdot v_t \quad (16)$$

$$v_t = u - v_{rc} \quad (17)$$

$$v_{rc} = \text{MRC}(q) \quad (18)$$

$$q = Tx + Cv_t \quad (19)$$

$$\dot{q} = \alpha |\dot{v}_{rc}| (\beta v_{rc} - q) + r \dot{v}_{rc}, \quad (20)$$

where F_t is the transducer force from the electrical domain, T is the electromechanical transformer ratio, C is the linear capacitance in parallel with the transformer, q is the total charge in the ceramic, v_t is the back-emf from the mechanical side, u is the actuator input voltage, v_{rc} is the voltage across the Maxwell resistive capacitance (which Eq. (18) indicates is a function of q). Combining Eqs. (16) and (17) gives the following dynamic equations of the PEA of the X and Y stage:

$$\begin{cases} m\ddot{x} + b\dot{x} + kx = T \cdot u - T \cdot v_{rc} & (a) \\ \dot{q} = \alpha |\dot{v}_{rc}| (\beta v_{rc} - q) + \gamma \dot{v}_{rc} & (b) \\ q = T \cdot x + C \cdot (u - v_{rc}) & (c). \end{cases} \quad (21)$$

Differentiating Eq. (21)(c) and substituting $\dot{q}(t)$ into Eq. (21)(b) gives

$$\begin{aligned} \dot{q} &= \alpha |\dot{v}_{rc}| (\beta v_{rc} - q) + \gamma \dot{v}_{rc} \\ &= T \cdot \dot{x} + C \cdot (\dot{u} - \dot{v}_{rc}) \\ &= \alpha |\dot{v}_{rc}| (\beta v_{rc} - T \cdot x - C \cdot (u - v_{rc})) + \gamma \dot{v}_{rc}. \end{aligned} \quad (22)$$

If $\dot{v}_{rc} \geq 0$, then

$$\dot{v}_{rc} = \frac{1}{\alpha(C + \beta) \cdot v_{rc} - \alpha Tx - \alpha Cu + (C + \gamma)} \cdot [T\dot{x} + C\dot{u}]. \quad (23)$$

If $\dot{v}_{rc} < 0$, then

$$\dot{v}_{rc} = \frac{1}{-\alpha(C + \beta) \cdot v_{rc} + \alpha Tx + \alpha Cu + (C + \gamma)} \cdot [T\dot{x} + C\dot{u}]. \quad (24)$$

Therefore,

$$\dot{v}_{rc} = \begin{cases} f_+(v_{rc}, x, u) \cdot (T\dot{x} + C\dot{u}), & \text{for } \dot{v}_{rc} \geq 0 \\ f_-(v_{rc}, x, u) \cdot (T\dot{x} + C\dot{u}), & \text{for } \dot{v}_{rc} < 0, \end{cases} \quad (25)$$

where $f_+(v_{rc}, x, u) = \frac{1}{-\alpha(C + \beta) \cdot v_{rc} + \alpha Tx + \alpha Cu + (C + \gamma)}$ and $f_-(v_{rc}, x, u) = \frac{1}{\alpha(C + \beta) \cdot v_{rc} - \alpha Tx - \alpha Cu + (C + \gamma)}$.

For Duhem model, the piezoelectric hysteresis force $F_h = T \cdot v_{rc}$ is

$$\dot{F}_h(t) = f(F_h(t), x(t), u(t)) \cdot g(\dot{x}(t), \dot{u}(t)). \quad (26)$$

Remark 1. Eqs. (11), (15) and (26) show that the Bouc–Wen, Dahl and Duhem models are special cases of GDM. The $\dot{F}_h(t)$ in the Bouc–Wen model depends only on $\dot{u}(t)$ but is independent of $\dot{x}(t)$. In the Dahl model, $\dot{F}_h(t)$ depends on $\dot{x}(t)$ but is independent of $\dot{u}(t)$. The Duhem model includes both electrical and mechanical domains, and $\dot{F}_h(t)$ depends on $\dot{x}(t)$ and $\dot{u}(t)$.

Fig. 1 shows that the Duhem model is a general model for piezo-electrical hysteresis, which consists of the interaction between electric and mechanical domains. The hysteresis force for Duhem model depends on the deformation of PA and the applied voltage, but the hysteresis force for Bouc–Wen model only depends on $\dot{u}(t)$ and it only depends on $\dot{x}(t)$ for OR PA deformation and applied voltage, but the hysteresis force depends only on $\dot{u}(t)$ in the Bouc–Wen model and depends only on $\dot{x}(t)$ in the Dahl model. The following experiments compare these three models in terms of their responses to different sinusoidal inputs.

3. Experimental test description and model identification

3.1. Experimental setup

In the proposed biaxial piezo-actuated FBM, which is actuated by two piezo-stack PAs, position feedback is provided by two optical encoders with linear glass scales. A wire electric-discharge-machine (WEDM) is used to fabricate the monolithic XY stage from a piece of A7075 material. Fig. 2 shows that the monolithic XY stage enables independent motion of the

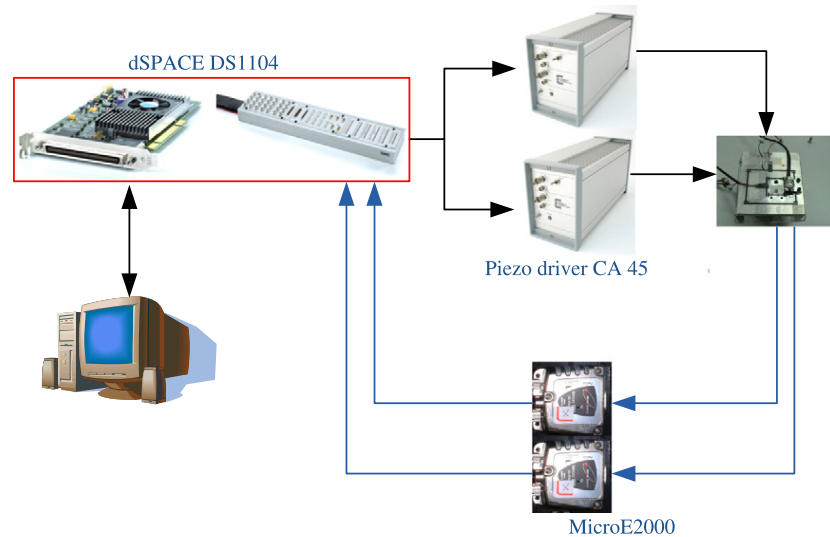


Fig. 4. Schematic diagram of the PA-actuated XY stage.

Table 1

The specification of the PA.

Type number	PSt 150/5 × 5/20
Ceramic cross section	5 mm × 5 mm
Length	18 mm
Max. stroke (No load) $(+)U_{\max} = 150$ V	20 μm
Capacitance	1800 nF
Resonance frequency	50 kHz
Stiffness	60 N/ μm
Blocking force	1600 N
Max. load force	2000 N

translation platform in the X and Y directions. An electrical voltage applied to the PA of X - or Y -axis increases the length of the PA and applies a force to the X - or Y - moving stages, respectively. This stage is driven by two 20 μm -stroke PZTs (model PSt 150/5 × 5/20, manufactured by Piezomechanik GmbH, Germany), which are actuated by two PZT drivers (voltage -20 to $+150$ V; model CA45, manufactured by CEDRAT, France). Tables 1 and 2 describe the specifications for the PZT and the PZT driver, respectively. Fig. 2 shows that the mechanical architecture of the piezo-actuated flexure-based mechanism (PAFBM) is equipped with an optical 0.1 μm resolution encoder (Mercury 2000, made by MicroE systems, USA) on each moving stage to provide position feedback. Fig. 3 shows top and bottom views of the PAFBM. The feedback signal of the optical encoder is 0.1 $\mu\text{m}/\text{count}$ and is decoded by the DSP controller (model: DS1104 PPC control board, made by dSPACE, Germany) to enable data acquisition and real-time control. The dSPACE DS1104 has a MPC8240 processor with PowerPC 603e core and a 250 MHz CPU clock. The dSPACE DS1104 board is equipped with 32 MB application memory for storing the real-time programs to be executed. Fig. 4 graphically depicts the experimental setup for this piezo-actuated positioning system. The dSPACE system combines software and hardware for real-time control. For the dSPACE system, the real-time implementation can be achieved using MATLAB Simulink to generate real-time executable codes. After successfully modeling the plant in Simulink, the simulation model can be used for automatically generating code for testing the control system using actual hardware. Real-Time Interface (RTI) is used to graphically configure all I/O, to insert the blocks into a Simulink block diagram, and to generate the model code via Real-Time Workshop[®]. Since the real-time model compiles, downloads, and starts automatically, implementation time is minimized.

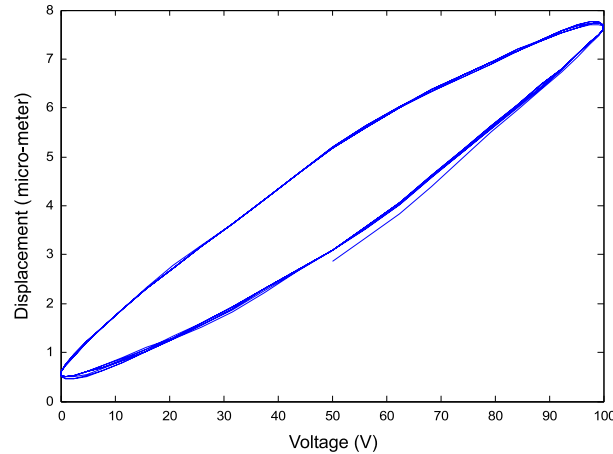
3.2. Hysteresis modeling

Section 2 above showed how nonlinear hysteresis effects on the piezoelectric material can be modeled and how the feed-forward system compensates for hysteresis based on the inverse-hysteresis model. The hysteresis models can be categorized as integral models and nonlinear differential models. Preisach model, the generalized Maxwell-slip model and the Prandtl–Ishlinskii model are integral hysteresis models that use different kernel functions. Preisach model is a popular hysteresis model because it captures a large class of hysteresis maps with complex reversal behavior. Because the kernel in its integral model involves an infinite number of hysteretic operators, however, numerous experimental results are needed to establish grids of the plane. As discussed in Section 2, the generalized Duhem models (GDMs) presented for the

Table 2

The specification of the compact amplifier CA45.

Properties	Nominal values	Unit
Main voltage	230 VAC 50 Hz	VAC/Hz
Input voltage (Min./Max.)	−1.2/7.7	V
Output voltage (Min./Max.)	−20/150	V
Gain	20	V/V
Max. output current	0.036	A
Max. output load capacitance	400	μF
Signal to noise ratio	85	dB
Input impedance	10	kΩ

**Fig. 5.** The hysteresis loop of the X-axis PAFBM.

three hysteresis models include the Dahl model, Bouc–Wen model and Duhem model. To compare how these three models respond to different inputs, a simulation model was established, and hysteresis parameters were identified.

3.2.1. Implementing GDM using Simulink model in the Bouc–Wen model

Consider the dynamic equation of PAFBM with Bouc–Wen hysteresis model. In the Simulink model shown in Fig. 6, the subsystem 1 block represents the dynamic FBM system as

$$m\ddot{x} + b\dot{x} + kx = F, \quad (27)$$

where x is the output displacement and F is the total force produced by PA as

$$F = kd_e u - F_h, \quad (28)$$

where d_e is the piezoelectric coefficient, u is the input voltage and F_h is the piezoelectric hysteresis force. Eq. (11) obtains F_h according to $\dot{u}(t)$. The coefficient of transition from elastic to plastic response is defined as $n = 1$ and parameters α , β , γ are used to control the amplitude and shapes of the hysteresis loop as shown in Eq. (10). Therefore, the relation between F_h and $u(t)$ can be established as the subsystem block in Fig. 6. The hysteresis model can be determined using seven parameters: m , b , k , d_e , α , β and γ .

3.2.2. Using Simulink to implement GDM for Dahl model

The dynamic equation of PAFBM with Dahl hysteresis model can be used to establish the Simulink model as shown in Fig. 7, where the subsystem block represents the dynamic system of FBM. According to Eq. (15), F_h can be determined according to $\dot{x}(t)$ as shown in the subsystem block in Fig. 7. The hysteresis model can be determined using seven parameters m , b , k , T , a_0 , a_1 and b_1 , where $b_0 = 0$ and $u_p = 30$ are as recommended in Ref. [8].

3.2.3. Implementation of GDM using Simulink model for Duhem model

Consider the dynamic equation of PAFBM with Duhem hysteresis model. The Simulink model can be established as shown in Fig. 8, where the subsystem block 1 represents dynamic system of FBM. According to Eqs. (23) and (24), Duhem model consists of both electric and mechanical domain and $\dot{F}_h(t)$ depends on $x(t)$ and $u(t)$. Therefore, its relation can be established as shown at the subsystem block in Fig. 8. The hysteresis model can be determined using seven parameters m , b , k , T , α , β and r .

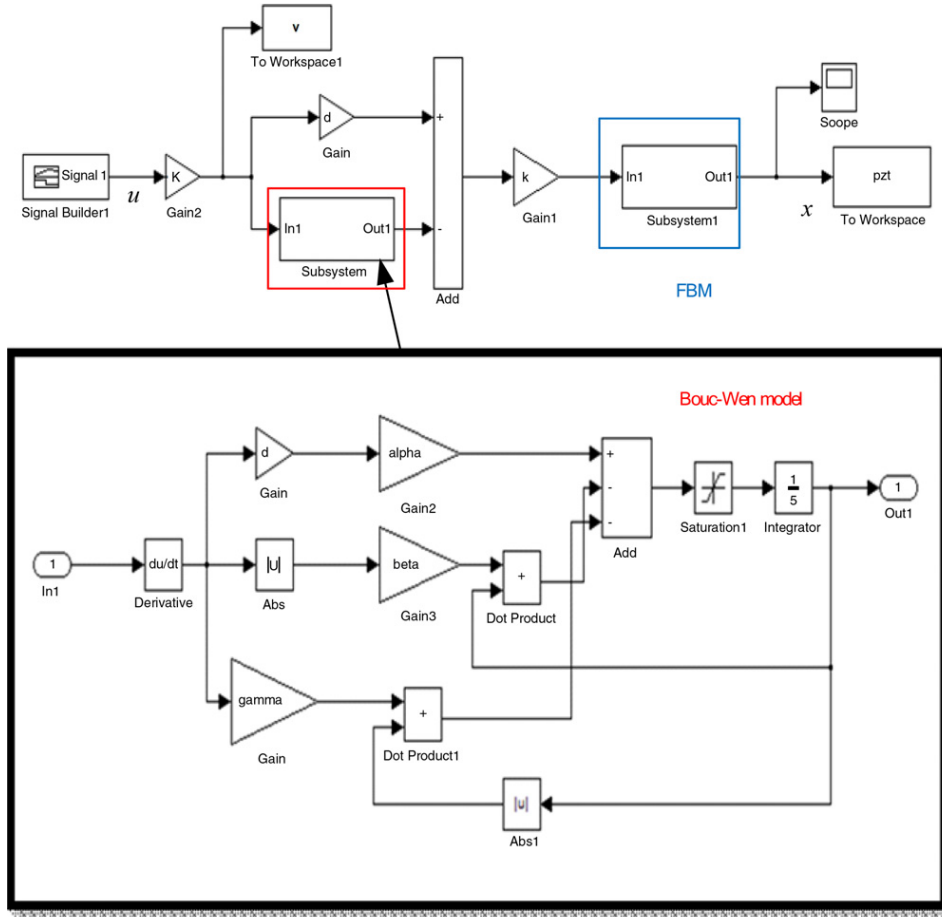


Fig. 6. The block diagram of the PAFBM using Bouc–Wen hysteresis model.

After implementing GDM for these three hysteresis models, system model parameters that are mainly attributable to hysteresis are identified. For example, since seven system parameters are needed, the magnitude of the hysteresis loops and the shape of the Duhem model are difficult to determine by trial and error. However, a preliminary simulation reveals that the output model identified by the conventional method does not closely match experimental results. Thus, an optimization problem is formulated to determine a set of model parameters in which the GDM output matches the minimum root-mean-square error (RMSE) in the experimental results.

3.3. The optimization problem for model identification

For a PEA, the relation between actuating force and applied voltage is a linear rather than a nonlinear hysteresis model. To establish the hysteresis model, the relation between the displacements and applied voltages must be measured to obtain the parameters for the nonlinear hysteresis model. To illustrate the optimization of the system model, the sinusoidal signal with a frequency of 8 Hz and an amplitude of 100 (V) is applied to Y-axis PA. Fig. 5 describes the hysteretic loop of the Y-axis stages via the measurement data of the optical encoders. To solve this problem, the hysteresis dynamics are established by GDM as mentioned above. Firstly, the optimization problem for these three models is formulated as described below. The parameters for the hysteresis system model are then optimized by particle swarm optimization (PSO).

(1) After applying Bouc–Wen model to describe the nonlinearity of PA, Eqs. (9) and (10) are used to construct the PAFBM model. The seven system parameters are m_i , b_i , k_i , d_{ei} , α_i , β_i , γ_i , where $i = 1, 2$ for X-axis and Y-axis stages, respectively. Without loss of generality, the optimization problem is formulated as follows with constraints.

$$\text{Min}_{\text{parameters}} J(x) = \sqrt{\frac{1}{N} \sum_{i=1}^N (x_h(i) - x(i))^2}. \quad (29)$$

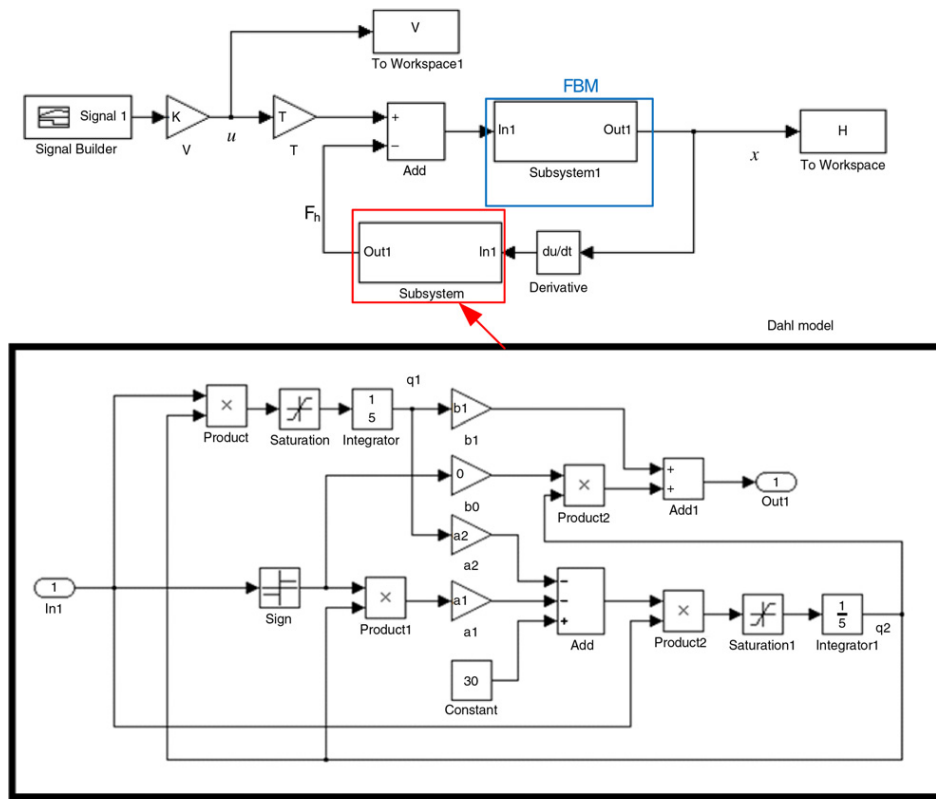


Fig. 7. The block diagram of the PAFBM using Dahl hysteresis model.

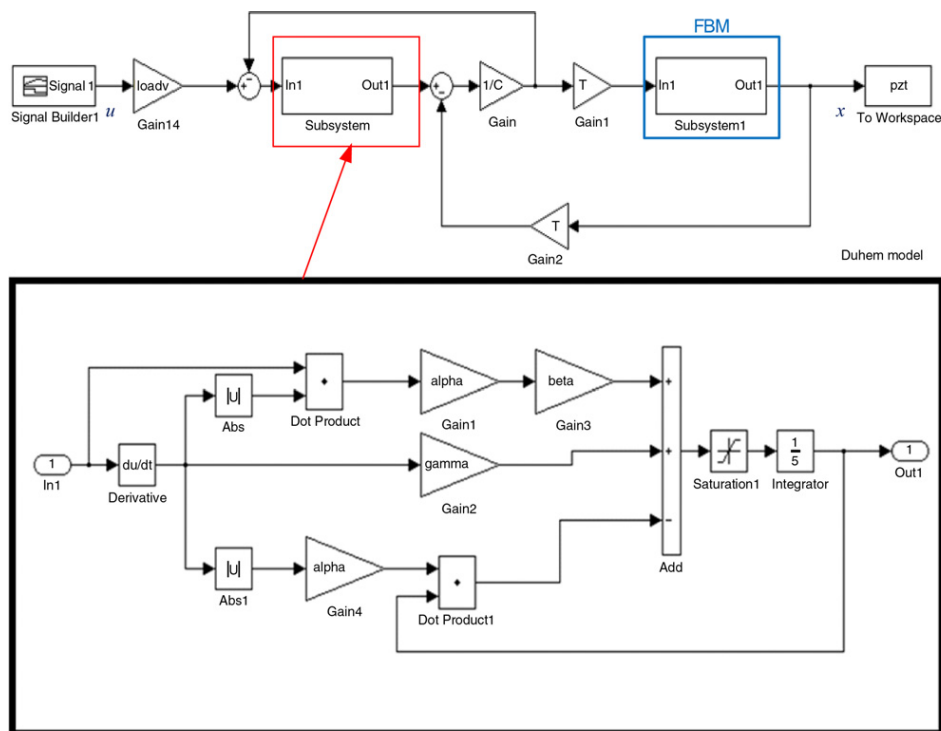


Fig. 8. The block diagram of the PAFBM using Duhem hysteresis model.

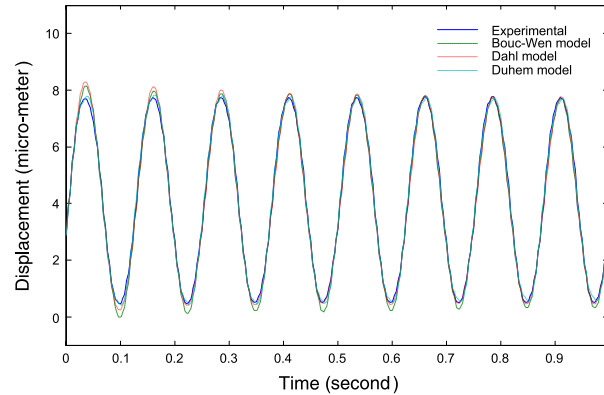


Fig. 9. The sinusoidal response and the modeling output using the variant hysteresis model, which are Bouc–Wen, Dahl and Duhem models.

Subject to:

$$\text{equality constraints : } \begin{cases} m_i \ddot{x} + b_i \dot{x} + k_i x = k_i d_{ei} u - F_h = k_i d_{ei} u - k_i \cdot h \\ \dot{h}(t) = \alpha_i \dot{u} - \beta_i |\dot{u}(t)| \cdot h(t) - \gamma_i \dot{u} |h(t)| \end{cases} \quad (30)$$

$$\text{inequality constraints : } \begin{cases} 0 \leq m_i \leq \bar{m}_i \\ 0 \leq b_i \leq \bar{b}_i \\ 0 \leq k_i \leq \bar{k}_i \\ 0 \leq d_{ei} \leq \bar{d}_{ei} \\ 0 \leq \alpha_i \leq \bar{\alpha}_i \\ 0 \leq \beta_i \leq \bar{\beta}_i \\ 0 \leq \gamma_i \leq \bar{\gamma}_i, \end{cases} \quad (31)$$

where $J(x)$ is the objective function; $x_h(i)$ represents the experimental value of the hysteric loop obtained via the measurement at the i th sampling time in Fig. 5; $x(i)$ are the calculated data via Eqs. (30) and (31) at the i th sampling time; and N is the total sampling number from the experimental results. In this optimization problem, the objective function $J(x)$ represents the root mean squared error (RMSE) between the experimental results and the simulation data.

(2) As mentioned above, the Dahl model was applied to describe the nonlinearity of the PA in Eqs. (13) and (14). To identify the seven system parameters $m_i, b_i, k_i, T_i, a_{0i}, a_{1i}$ and b_{1i} , where $i = 1, 2$ for X-axis and Y-axis stages, the optimization problem is as follows with constraints.

$$\text{Min}_{\text{parameters}} J(x) = \sqrt{\frac{1}{N} \sum_{i=1}^N (x_h(i) - x(i))^2} \quad (32)$$

subject to:

$$\text{equality constraints : } \begin{cases} m_i \ddot{x} + b_i \dot{x} + k_i x = F_d - F_h = T_i \cdot u(t) - C_h \cdot V \\ \dot{V}(t) = A_h V \cdot \dot{x} + B_h u_p \cdot \dot{x} \end{cases} \quad (33)$$

$$\text{inequality constraints : } \begin{cases} 0 \leq m_i \leq \bar{m}_i \\ 0 \leq b_i \leq \bar{b}_i \\ 0 \leq k_i \leq \bar{k}_i \\ 0 \leq T_i \leq \bar{T}_i \\ 0 \leq a_{0i} \leq \bar{a}_{0i} \\ 0 \leq a_{1i} \leq \bar{a}_{1i} \\ 0 \leq b_{1i} \leq \bar{b}_{1i}, \end{cases} \quad (34)$$

where $V = [q_1 \ q_2]^T$ is state vector for the second-order model, $u_p = 30$ is recommended as a constant in Ref. [18], and A_h, B_h, C_h are $A_h = \begin{bmatrix} 0 & 1 \\ -a_2 & -\text{sgn}(\dot{x})a_1 \end{bmatrix}$, $B_h = \begin{bmatrix} 0 \\ 1 \end{bmatrix}$, $C_h = [b_1 \ \text{sgn}(\dot{x})b_o]$; $J(x)$ is the objective function; the $x_h(i)$ represents the experimental data of the hysteric loop via the measurement at the i th sampling time in Fig. 5; $x(i)$ are the calculated data via Eqs. (33) and (34) at the i th sampling time; N is the total sampling number from the experimental results.

(3) The Duhem model was applied to describe the nonlinearity of the PA in Section 2.2.3; the PAFBM model was constructed using Eq. (21). To identify the seven system parameters $m_i, b_i, k_i, T_i, \alpha_i, \beta_i$ and r_i , where $i = 1, 2$ for X-axis and Y-axis stages, the optimization problem with constraints is formulated as.

$$\text{Min}_{\text{parameters}} J(x) = \sqrt{\frac{1}{N} \sum_{i=1}^N (x_h(i) - x(i))^2}. \quad (35)$$

Subject to:

$$\text{equality constraints : } \begin{cases} m_i \ddot{x} + b_i \dot{x} + k_i x = T_i \cdot u - T_i \cdot v_{rc} \\ \dot{q} = \alpha_i |\dot{v}_{rc}| (\beta_i v_{rc} - q) + \gamma_i \dot{v}_{rc} \\ u - v_{rc} = \frac{q - T_i \cdot x}{C} \end{cases} \quad (36)$$

$$\text{inequality constraints : } \begin{cases} 0 \leq m_i \leq \bar{m}_i \\ 0 \leq b_i \leq \bar{b}_i \\ 0 \leq k_i \leq \bar{k}_i \\ 0 \leq T_i \leq \bar{T}_i \\ 0 \leq \alpha_i \leq \bar{\alpha}_i \\ 0 \leq \beta_i \leq \bar{\beta}_i \\ 0 \leq \gamma_i \leq \bar{\gamma}_i, \end{cases} \quad (37)$$

where C is the capacitance of the PA, q is the total charge in the ceramic, v_t is the back-emf from the mechanical side, u is the actuator input voltage, and v_{rc} is the voltage across the Maxwell resistive capacitance. The accuracy of the estimated hysteresis model increases only after a large decrease in the value of $J(x)$. Therefore, particle swarm optimization is applied as described in the next section.

3.4. Model identification using particle swarm optimization

The goal of optimization described in Section 3.3 is to optimize the parameter set so that the GDM output is consistent with the experimental results with minimum deviation. The optimization problem for this nonlinear hysteresis model does not require an analytical expression for the objective function. Thus, this nonlinear discontinuous optimization problem cannot be solved by a standard successive dynamic programming algorithm that uses a local search procedure based on the gradient of cost function. Since conventional direct search methods such as Nelder–Mead simplex algorithm are sensitive to the initial search point, they may fall into local optima if the starting points approach the local optima. In contrast, the PSO global search method can solve both constrained and unconstrained optimization problems. In the mid 1990s, Eberhart and Kennedy developed particle swarm optimization (PSO), an alternative method of modeling complex non-linear optimization problems by using the boids method developed by Craig Reynolds to model the collective behavior of bird flocks, particles [26]. The PSO shares many similarities with evolutionary computation techniques such as GAs. After the system is initialized with a population of random solutions, it searches for optima by updating generations. Unlike GA, however, PSO has no evolution operators such as crossover and mutation.

The PSO is a multi-agent parallel search technique. Particles are conceptual entities that fly through the multi-dimensional search space. At any particular instant, each particle has a position and a velocity. The position vector of a particle with respect to the origin of the search space represents a trial solution of the search problem. First, a population of particles is initialized with random positions marked by vectors \bar{x}_i and random velocities \bar{v}_i . The population of such particles is called a “swarm”. Each particle has two state variables, its current position $\bar{x}_i(t)$ and its current velocity $\bar{v}_i(t)$. Each particle is also equipped with a small memory comprising its previous best position $\bar{p}(t)$, which is the personal best experience and the best of all particles so far, and the best value so far in the group among the best position $\bar{g}(t)$, which is referred to as the globally best particle in the entire swarm. The global version of PSO is implemented as follows:

- (1) Initialize a population of particles with random positions and velocities in d dimensions in the problem space.
- (2) For each particle, evaluate the desired optimization fitness function in d variables.
- (3) For each particle, compare the fitness evaluation particle with the $pbest$. If the current value is better than $pbest$, set the $pbest$ value to equal the current value, and set the $pbest$ location to equal the current location in d dimensional space.
- (4) Compare fitness evaluation with the best evaluation observed previously in the overall population. If the current value is better than $gbest$, then reset $gbest$ to the array index and value of the current particle.
- (5) Change the velocity and position of the particle using the following equations:

$$v_{id}(t+1) = v_{id} + c_1 \times \text{rand}() \times (p_{id}(t) - x_{id}(t)) + c_2 \times \text{rand}() \times (g_{id}(t) - x_{id}(t)) \quad (38)$$

$$x_{id}(t+1) = x_{id}(t) + v_{id}(t+1). \quad (39)$$

- (6) Loop to step II until a criterion is met, usually a sufficiently good fitness or maximum number of iterations.

Table 3
The searching range for the parameters of the system.

Parameters	Search range	Optimal parameters
m_1 (kg)	0.15–0.17	0.1600
b_1 (N s/m)	0–10	0.0000
k_1 (N/m)	7×10^7 – 8×10^7	7.9993E7
d_1 (m/V)	0–5E–7	1.0566E–7
α_1	0–1	0.4288
β_1	0–1	0.0412
γ_1	0–1	0.0205

Clamp the velocities of the particles in each dimension to a maximum velocity V_{\max} . If the sum of accelerations causes the velocity in that dimension to exceed parameter V_{\max} specified by the user, then the velocity in that dimension is limited to V_{\max} .

The V_{\max} is therefore an important parameter because it determines the resolution, or fitness, with which regions between the present and targeted positions are searched. If V_{\max} is too high, particles might fly past good solutions. If V_{\max} is too small, however, particles may not sufficiently explore beyond local good regions. The acceleration constants c_1 and c_2 in Eq. (38) represent the weighting of the stochastic acceleration terms that pull each particle toward $pbest$ and $gbest$ positions, respectively.

In 2002, Clerc and Kennedy proposed an adaptive PSO model [27] that uses a new parameter ‘ χ ’ called the constriction factor. Constriction coefficient enable rapid convergence of particles over time. That is, the amplitude of oscillations of a particle decreases as the particle focuses on the local and neighborhood previous best points. Although the particle converges to a point over time, the constriction coefficient also prevents collapse if the right social conditions are in place. The particle oscillates around the weighted mean of $\bar{p}(t)$ and $\bar{g}(t)$, and if the previous best position and the neighborhood best position are near each other, the particle performs a local search. The constriction coefficient method therefore balances the need for local and global search depending on the social conditions in place. Initially, the settings for $\bar{p}(t)$ and $\bar{g}(t)$ are $\bar{p}(0) = \bar{g}(0) = \bar{x}(0)$ for all particles. Once all particles are initialized, an iterative process optimizes the positions and velocities of all particles according to the following recursive equations:

$$v_{id}(t+1) = \chi [v_{id} + c_1 \times \varphi_1 \times (p_{id}(t) - x_{id}(t)) + c_2 \times \varphi_2 \times (g_{id}(t) - x_{id}(t))] \quad (40)$$

$$x_{id}(t+1) = x_{id}(t) + v_{id}(t+1), \quad (41)$$

where

$$\chi = \frac{2}{4 - \phi - \sqrt{\phi^2 - 4\phi}} \quad \text{with } \phi = c_1 + c_2. \quad (42)$$

Since coefficient c_1 contributes to the self-exploration of a particle, coefficient c_1 is considered the self-confidence of the particle. The contribution of coefficient c_2 to motion of the particles depends on the motion of all the particles in the preceding program iterations, so its definition as “swarm confidence” is apparent. Coefficients φ_1 and φ_2 represent uniformly distributed random numbers in the interval [0, 1]. The first iteration of the algorithm is completed when the velocities and position for the next time step $t+1$ are calculated.

3.5. Model identification and discussions for case studies

For this PAFBM, the relation between actuating force and applied voltage is a nonlinear rather than linear hysteresis model. The parameters of the hysteresis model are obtained by measuring the relation between the displacements and applied voltages. To obtain the hysteretic loop needed to compare three hysteresis models, consider the following input sinusoidal signal.

$$u(t) = 50 + 50 \sin 16\pi t. \quad (43)$$

Eq. (43) formulates the input voltage as a sinusoidal waveform with frequency 8 Hz and amplitude 100 (V), which is applied to the X-axis PA. Fig. 5 describes the hysteretic loop of the X-axis stage using the measurement data of the optical encoders. To identify the parameters of the nonlinear differential equations as described in Section 3.3, three PSO case studies are used to optimize the parameters for Bouc–Wen model, Dahl model and Duhem model. For these three case studies of model identification, Tables 3–5 describes the range of system parameters for Bouc–Wen model, Dahl model and Duhem model. In the preliminary study, PSO parameters are designed as follows: the acceleration constants are $c_1 = 2.8$ and $c_2 = 1.3$; the constriction factor of PSO is $\chi = 0.729843$ and the number of generations is 250.

Case I.

Table 3 presents the search ranges of $m_1, b_1, k_1, d_1, \alpha_1, \beta_1, \gamma_1$ of Bouc–Wen model; Table 4 shows the search ranges of $m_1, c_1, k_1, T_1, a_{11}, a_{21}, b_{11}$ for Dahl model, and Table 5 shows the search ranges for $m_i, c_i, k_i, T_i, \alpha_i, \beta_i, \gamma_i$ for Duhem model. The PSO method is used to optimize the hysteresis system parameters for the Bouc–Wen model. Table 3 also shows the

Table 4

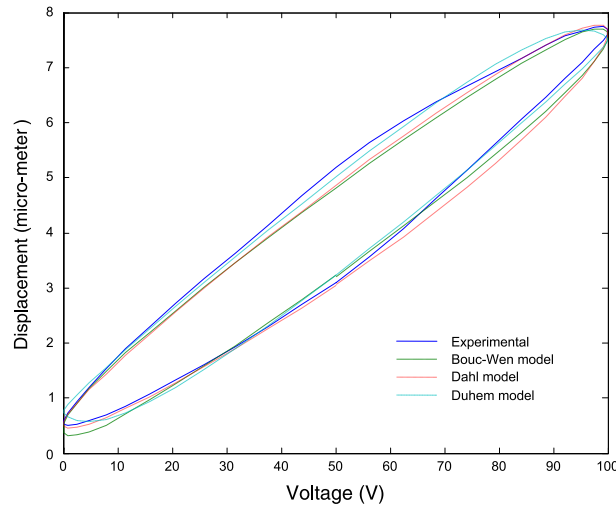
The searching range for the parameters of the Dahl model.

Parameters	Search range	Optimal parameters
m_1 (kg)	0.15–0.17	0.1516
b_1 (N s/m)	0–10	0.0000
k_1 (N/m)	7×10^7 – 8×10^7	7.788E7
T_1 (C/m)	0–50	6.193483
a_{11}	1E4–1E7	2.0714E4
a_{21}	1E8–1E14	4.055E9
b_{11}	1E8–1E14	4.420E10

Table 5

The searching range for the parameters of the system.

Parameters	Search range	Optimal parameters
m_1 (kg)	0.15–0.17	0.1527
b_1 (N s/m)	0–10	0.0000
k_1 (N/m)	7×10^7 – 8×10^7	7.0019E7
T_1 (C/m)	0–50	30.0000
α_1	0–1	0.0546
β_1	1×10^{-8} – 1×10^{-4}	3.6252E–6
γ_1	1×10^{-8} – 1×10^{-4}	2.0357E–6

**Fig. 10.** The hysteresis loop for actual response and the variant hysteresis models.

simulation results obtained for the Bouc–Wen model with the reference input in Eq. (43). The simulation results of Simulink code when using the optimal parameters are then used to compare the displacement output of PAFBM using Bouc–Wen model, Dahl model and Duhem model with the actual displacement in Fig. 9. Fig. 10 shows the hysteresis loops for the actual response and the Bouc–Wen model, the Dahl model and the Duhem model. According to the resulting response of Bouc–Wen model, there exists a transient response, and the maximal modeling error approximates $0.51 \mu\text{m}$. When the system stabilizes, the RMSE for Bouc–Wen model approximates $0.08665 \mu\text{m}$. In the Dahl model, the maximal transient error is about $0.72 \mu\text{m}$ and the steady-state RMSE is about $0.09048 \mu\text{m}$. In the Duhem model, the maximal transient error is about $0.11 \mu\text{m}$ and the steady-state error approximates $0.08480 \mu\text{m}$. The response of the Bouc–Wen model is worse than that of the Dahl model, which is consistent with the results reported in Ref. [8]. However, comparison of the responses of Bouc–Wen model and Dahl model shows that the Duhem model has the best transient and steady-state response for hysteresis modeling because, as discussed in Section 2, it includes both electric and mechanical domains.

4. Controller design for the biaxial PAFBM based on Duhem model

Section 3 hypothesized that the X-stage and Y-stage are not actuated simultaneously and that each stage works in the standalone mode. Therefore, the cross-coupling effect between the X- and Y-axis is negligible. The Duhem model therefore has the best modeling performance for this PAFBM as only one PA is used to actuate the X-axis FBM. After studying the standalone driving model, the simultaneous driving model for this PAFBM is considered. The cross-coupling effect between

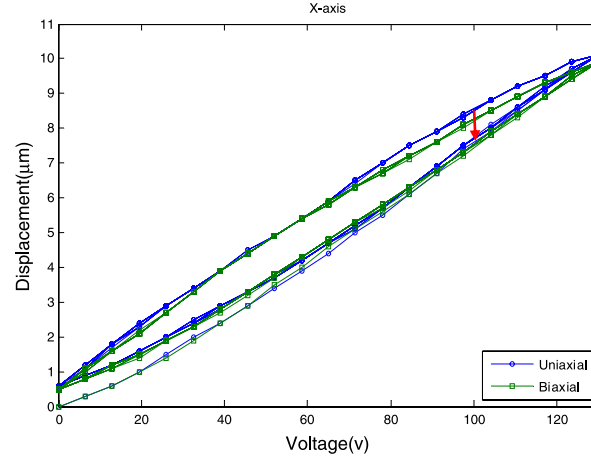


Fig. 11. The hysteresis loop by biaxial actuated and uniaxial actuated of X-axis.

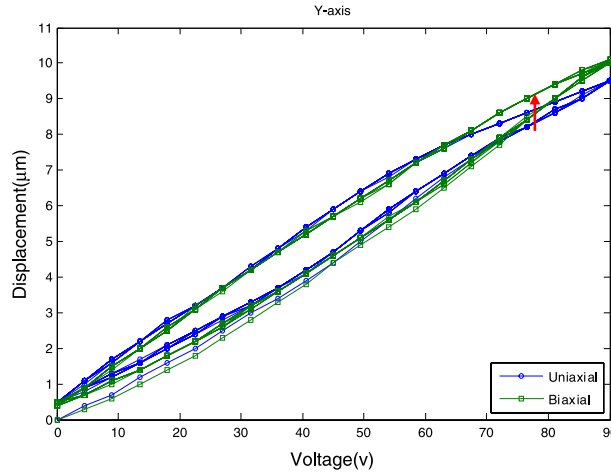


Fig. 12. The hysteresis loop by biaxial actuated and uniaxial actuated of Y-axis.

the X- and Y-axes should then be considered, and the general dynamic equations of biaxial PA XY-biaxial positioning stage are described as follows [21].

$$\begin{bmatrix} m_{11} & 0 \\ 0 & m_{22} \end{bmatrix} \begin{bmatrix} \ddot{x}_1 \\ \ddot{x}_2 \end{bmatrix} + \begin{bmatrix} b_{11} & 0 \\ 0 & b_{22} \end{bmatrix} \begin{bmatrix} \dot{x}_1 \\ \dot{x}_2 \end{bmatrix} + \begin{bmatrix} k_{11} & 0 \\ 0 & k_{22} \end{bmatrix} \begin{bmatrix} x_1 \\ x_2 \end{bmatrix} = \begin{bmatrix} k_{11} & k_{12} \\ k_{21} & k_{22} \end{bmatrix} \begin{bmatrix} d_1 \cdot u_1 - h_1 \\ d_2 \cdot u_2 - h_2 \end{bmatrix}, \quad (44)$$

where x_1 and x_2 are the displacements of the X and Y-stages, respectively; m is the mass, b is the viscous damping, k is the spring stiffness, d is the piezoelectric coefficient, u is the input voltage and h is the hysteresis state. The subscripts 1 and 2 represent the parameters in the X- and Y-directions, respectively. For example, k_{11} is the spring stiffness for X displacement with respect to X-axis force $f_{pz1} = k_1(d_1 \cdot u_1 - h_1)$; k_{21} is the cross-coupling term of the spring stiffness for Y displacement with respect to X-axis force f_{pz1} . To establish the feedforward controller for the biaxial PAFBM, the next section discusses the model identification for this system with cross-coupling terms.

4.1. Model identification for the biaxial PAFBM with cross-coupling term

In the biaxial actuated FBM, triangle waveforms with input voltages of 130 and 90 (V) at 10 Hz frequency are respectively applied to the X-axis and Y-axis PAs. Biaxial actuated hysteresis loops are then compared with uniaxial actuated hysteresis loops. Figs. 11–12 show that cross-coupling occurs when the X-axis and Y-axis PEA stage are actuated simultaneously. Therefore, the proposed Duhem model with cross-coupling terms compensates for cross-coupling as follows.

$$\begin{cases} m_1 \ddot{x}_1 + b_1 \dot{x}_1 + k_{11} x_1 = v_{t1} T_1 - k_{12} x_2 \\ \dot{q}_1(t) = \alpha_1 |\dot{v}_{rc1}| (\beta_1 v_{rc1} - q_1) + \gamma_1 \dot{v}_{rc1} \end{cases} \quad (45)$$

Table 6

The comparison of RMSE and maximal modeling error for the variant hysteresis models.

Model	RMSE (μm)	Maximal error (μm)
Bouc–Wen	0.08665	0.51
Dahl	0.09048	0.72
Duhem	0.08480	0.11

$$\begin{cases} m_2 \ddot{x}_2 + b_2 \dot{x}_2 + k_{22} x_2 = v_{r2} T_2 + k_{21} x_1 \\ \dot{q}_1(t) = \alpha_1 |\dot{v}_{rc1}| (\beta_1 v_{rc1} - q_1) + \gamma_1 \dot{v}_{rc1}, \end{cases} \quad (46)$$

where k_{11} and k_{22} are the spring stiffnesses of X- and Y-axis stages, and k_{12} and k_{21} are the cross-coupling spring stiffnesses between X- and Y-axis stages, respectively. The $k_{12}x_2$ is the acting force at X-axis stage resulting from movement of the Y-axis stage, and $k_{21}x_1$ is the acting force at Y-axis stage resulting from movement of the X-axis stage. Eqs. (45) and (46) are then solved to simulate the hysteresis with the biaxial driving mode using PSO method. For each X-axis or Y-axis stage, the mass, damping coefficients, spring constants and piezoelectric constants (m_{11} , m_{22} , b_{11} , b_{22} , k_{11} , k_{22} , T_1 , T_2) are obtained by PSO, and cross-coupling effects assumedly have no influence on them. The forces generated by the X-axis or Y-axis PAs affect both FBM stages through stiffnesses k_{12} and k_{21} . Therefore, the optimization problem can be simplified as a search for eight cross-coupling response parameters. The optimization for biaxial PAFBM system is formulated as follows.

$$\begin{aligned} \text{Min}_{k_{12}, k_{21}, \alpha_1, \beta_1, \gamma_1, \alpha_2, \beta_2, \gamma_2} J(x) &= \sqrt{\frac{(\text{RMSE}_x)^2 + (\text{RMSE}_y)^2}{2}} \\ \text{subject to :} \end{aligned} \quad (47)$$

equality constraints:

$$\begin{bmatrix} m_1 & 0 \\ 0 & m_2 \end{bmatrix} \begin{bmatrix} \ddot{x}_1 \\ \ddot{x}_2 \end{bmatrix} + \begin{bmatrix} b_1 & 0 \\ 0 & b_2 \end{bmatrix} \begin{bmatrix} \dot{x}_1 \\ \dot{x}_2 \end{bmatrix} + \begin{bmatrix} k_{11} & 0 \\ 0 & k_{22} \end{bmatrix} \begin{bmatrix} x_1 \\ x_2 \end{bmatrix} = \begin{bmatrix} T_1 & 0 \\ 0 & T_2 \end{bmatrix} \begin{bmatrix} u_1 - v_{rc1} \\ u_2 - v_{rc2} \end{bmatrix} + \begin{bmatrix} 0 & -k_{12} \\ k_{21} & 0 \end{bmatrix} \begin{bmatrix} x_1 \\ x_2 \end{bmatrix} \quad (48)$$

$$\begin{cases} \dot{q}_1 = \alpha_1 |\dot{v}_{rc1}| (\beta_1 v_{rc1} - q_1) + \gamma_1 \dot{v}_{rc1} \\ \dot{q}_2 = \alpha_2 |\dot{v}_{rc2}| (\beta_2 v_{rc2} - q_2) + \gamma_2 \dot{v}_{rc2} \end{cases} \quad (49)$$

$$\begin{cases} u_1 - v_{rc1} = \frac{q_1 - T_1 \cdot x_1}{C_1} \\ u_2 - v_{rc2} = \frac{q_2 - T_2 \cdot x_2}{C_2}. \end{cases} \quad (50)$$

Inequality constraints:

$$\begin{cases} 0 \leq k_{12} \leq \overline{k_{12}} \\ 0 \leq k_{21} \leq \overline{k_{21}} \\ 0 \leq \alpha_1 \leq \overline{\alpha_1} \\ 0 \leq \beta_1 \leq \overline{\beta_1} \\ 0 \leq \gamma_1 \leq \overline{\gamma_1} \\ 0 \leq \alpha_2 \leq \overline{\alpha_2} \\ 0 \leq \beta_2 \leq \overline{\beta_2} \\ 0 \leq \gamma_2 \leq \overline{\gamma_2}, \end{cases} \quad (51)$$

where $J(x)$ is the objective function; and RMSE_x and RMSE_y represent the root mean square errors with respect to experimental data of the hysteresis loop via the measurement for the X- and Y- axes, respectively. Fig. 13 shows the Simulink model for the proposed Duhem model with cross-coupling term, and Table 7 describes the searching range for the inequality constraints and the optimal system parameters obtained by the PSO method. After system identification by PSO is complete, the parameters for the biaxial actuated Duhem model can be optimized. Table 8 shows the RMSE values for the simulation results. The simulation results in Table 8 clearly show that the proposed Duhem model has almost the same modeling errors as those shown in Table 6 for standalone mode. Therefore, the compensation with the cross-coupling term is effective for the simultaneous driving mode. The next section verifies the effectiveness of the proposed model implemented with real-time feedforward control using the optimal parameters obtained by PSO. To verify the effectiveness of the proposed model, the next section implements real-time feedforward control using the optimal parameters obtained by PSO.

4.2. Feedforward controller design and PI feedback compensation

Identification of the optimal parameters of the hysteresis model as described above enables estimation of the hysteresis term of the PA and FBM parameters. A feed-forward controller must be designed to compensate for nonlinearity caused

Table 7
The searching range for the parameters of the system.

Parameters	Range
k_{12}, k_{21} (N/m)	$1 \times 10^5 - 1 \times 10^7$
α_1, α_2	0–1
β_1, β_2	$1\text{E}-8 - 1\text{E}-4$
γ_1, γ_2	$1\text{E}-8 - 1\text{E}-4$

Table 8
The identified values of Duhem model with respect to the sinusoidal signal.

Parameters	α_1	β_1	γ_1	α_2	β_2	γ_2	k_{12}	k_{21}
Optima value	0.0323	$3.53\text{E}-6$	$2.48\text{E}-6$	0.0752	$5.58\text{E}-6$	$3.43\text{E}-6$	$3.1978\text{E}6$	$1.0024\text{E}6$
Stage	X-axis	Y-axis						
RMSE (μm)	0.08023	0.08500						

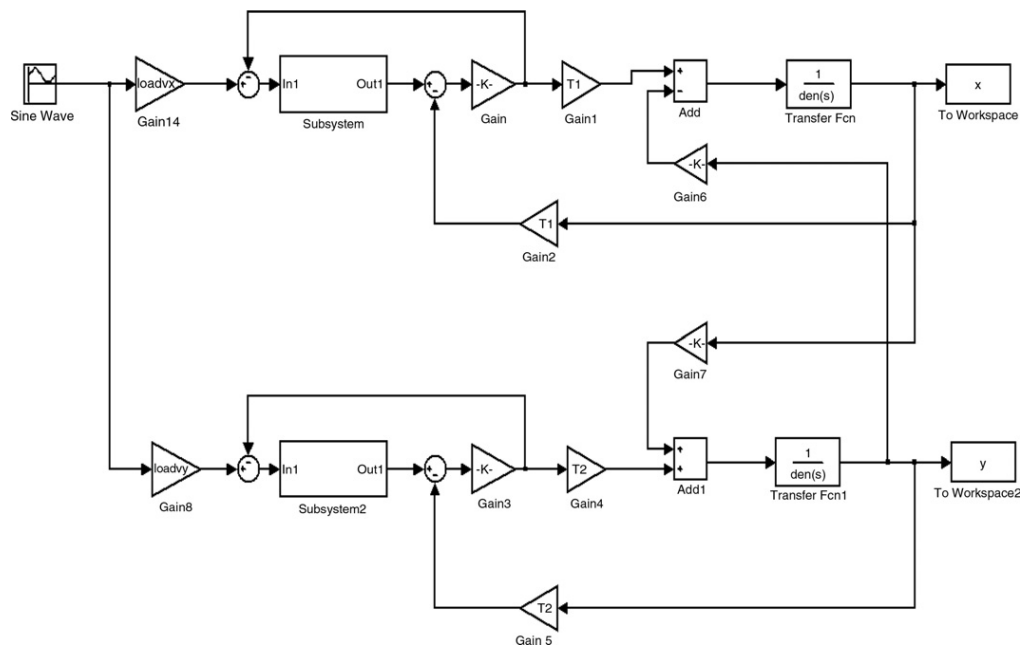


Fig. 13. The block diagram for the XY PAFBM using Duhem model with cross-coupling compensation.

by the hysteresis of the PA. Model-based feedforward control has proven effective for this purpose [23,28]. When using the atomic force microscope, the x -axis is operated at high frequencies during scanning, and both dynamic and hysteresis feedforward compensation is needed. However, the closed-loop integral control is used for the low-speed y -axis to minimize hysteresis and creep effects [23,28].

For the feedforward compensation based on Duhem model proposed in this study, the procedure for obtaining the feedforward compensation for X -axis is illustrated first. If the desired output trajectory $x_{d1}(t)$ is chosen as a sinusoidal wave, the feedforward compensation based on inverse Duhem hysteresis can be obtained as follows.

$$U_{ff1}(j\omega) = H^{-1}(j\omega)X_{d1}(j\omega),$$

where $X_{d1}(j\omega)$ is the Fourier transform of the desired output trajectory and $H^{-1}(j\omega)$ is the inverse of the Duhem hysteresis model, the inverse relation between $x_{d1}(t)$ and $u_1(t)$ can be obtained as follows.

- (1) Substitute the value of x_{d1} into the following dynamic equations in Eq. (52), which is obtained from Eq. (48), to obtain the value of $u_1 - v_{rc1}$.

$$\begin{aligned} & \begin{bmatrix} m_1 & 0 \\ 0 & m_2 \end{bmatrix} \begin{bmatrix} \ddot{x}_1 \\ \ddot{x}_2 \end{bmatrix} + \begin{bmatrix} b_1 & 0 \\ 0 & b_2 \end{bmatrix} \begin{bmatrix} \dot{x}_1 \\ \dot{x}_2 \end{bmatrix} + \begin{bmatrix} k_{11} & 0 \\ 0 & k_{22} \end{bmatrix} \begin{bmatrix} x_1 \\ x_2 \end{bmatrix} - \begin{bmatrix} 0 & -k_{12} \\ k_{21} & 0 \end{bmatrix} \begin{bmatrix} x_1 \\ x_2 \end{bmatrix} \\ &= \begin{bmatrix} T_1 & 0 \\ 0 & T_2 \end{bmatrix} \begin{bmatrix} u_1 - v_{rc1} \\ u_2 - v_{rc2} \end{bmatrix}, \end{aligned} \quad (52)$$

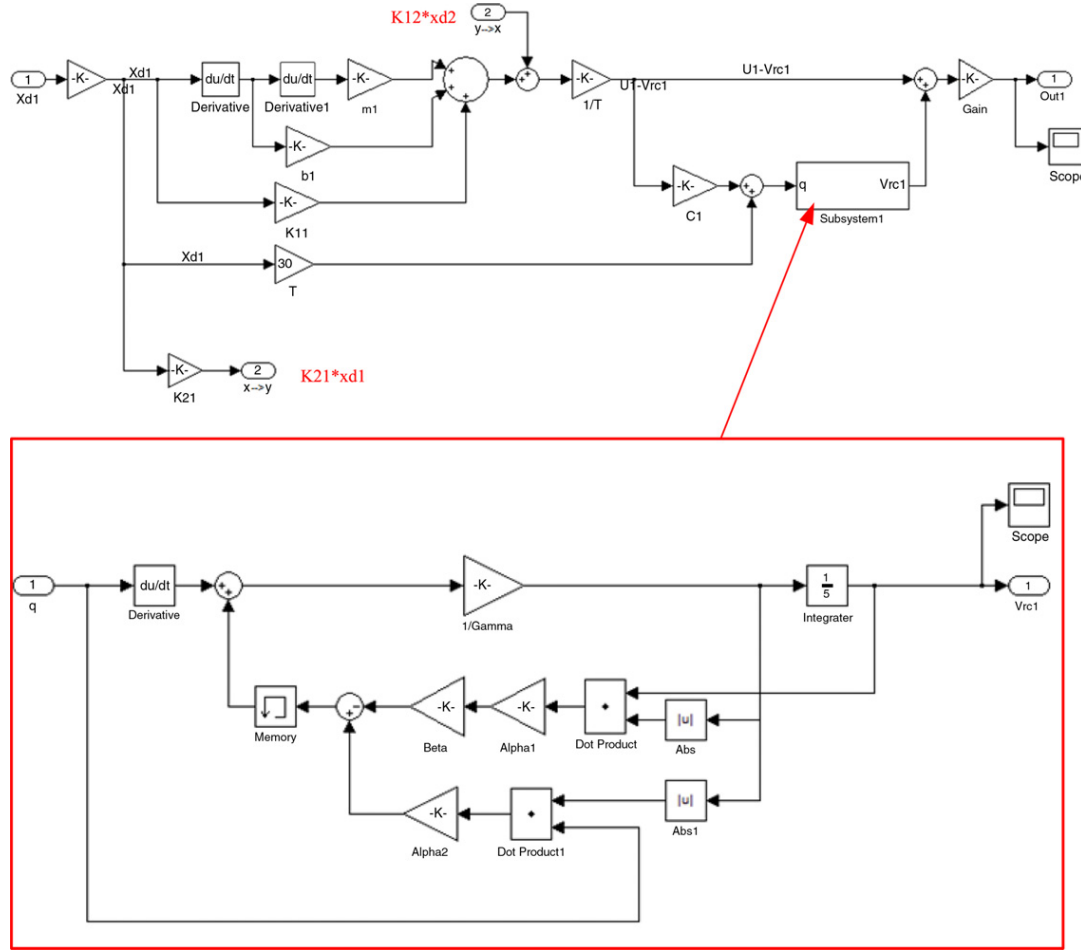


Fig. 14. The Simulink code for the proposed feedforward control based on Duhem model with cross-coupling compensation.

or

$$u_1 - v_{rc1} = \frac{1}{T_1} [(m_1 \ddot{x}_{d1} + b_1 \dot{x}_{d1} + k_{11} x_{d1}) + k_{12} x_{d2}], \quad (53)$$

where $k_{12} x_{d2}$ is the cross-coupling term, which is the interaction force from the Y -axis stage.

(2) Obtain q_1 from Eq. (50) as follows

$$q_1 = C_1 (u_1 - v_{rc1}) + T_1 \cdot \dot{x}_{d1}. \quad (54)$$

(3) Obtain v_{rc1} using the dynamic equations in (49) as follows.

$$\begin{cases} \alpha_1 |\dot{v}_{rc1}| (\beta_1 v_{rc1} - q_1) + \gamma_1 \dot{v}_{rc1} = \dot{q}_1 \\ \alpha_2 |\dot{v}_{rc2}| (\beta_2 v_{rc2} - q_2) + \gamma_2 \dot{v}_{rc2} = \dot{q}_2. \end{cases} \quad (55)$$

(4) Finally, the feedforward compensation u_{ff1} is the superposition of $u_1 - v_{rc1}$ in Step 1 and v_{rc1} in Step 3; the Simulink code for this inverse hysteresis compensation based on Duhem model can then be established as shown in Fig. 14.

For the Y -axis stage, the feedforward compensation resembles the X -axis. Modeling uncertainties and external disturbances causes tracking errors when only feedforward controls and no feedback controls are applied in this PAFBM system. Therefore, the feedback controller is needed to enhance system robustness and to improve tracking performance. A proportional–integral–derivative controller (PID controller) is the most common feedback controller used in industrial control systems. The characteristics of the PA cause the derivative controller to destabilize the PA system. Therefore, a PI controller is used as a feedback controller, and the total controller is

$$u'_1(t) = u_{ff1} + K_{p1} \cdot e_1(t) + K_{I1} \cdot \int_0^t e_1(t) dt \quad (56)$$

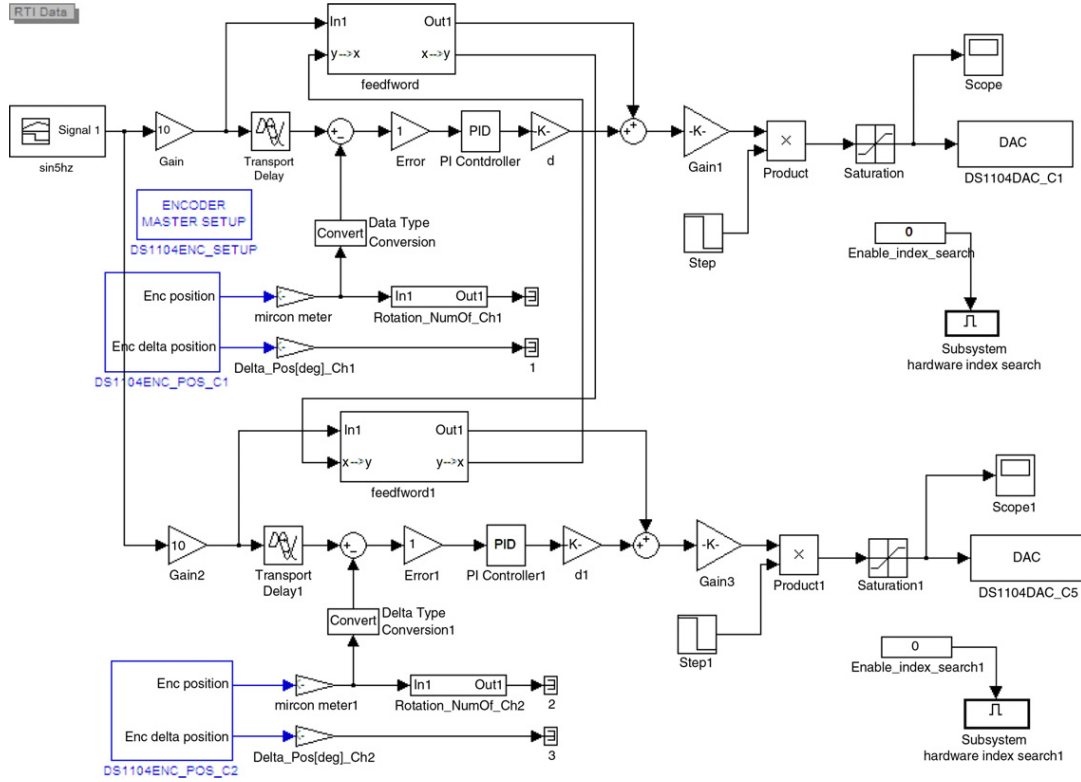


Fig. 15. The real-time Simulink code for the XY PAFBM using Duhem model with cross-coupling compensation.

where $e_1(t) = x_{d1}(t) - x_1(t)$ represents the positioning error of the system with feed-forward compensation for inverse hysteresis. If compensation by the feedforward controller results in a very small tracking error, the PI controller can be tuned by Ziegler–Nichols method [29–31].

4.3. Implementation with real-time control and discussions

Sections 4.1–4.3 proposed the feedforward controller based on Duhem model with the cross-coupling term. This section describes how the DS1104 PPC control board (dSPACE, Germany) is used as the real-time controller to achieve the proposed feed-forward control with the PI feedback controller. Fig. 15 describes the control scheme and the embedded Simulink code, where the feedforward block for the X-axis is as described in Fig. 14 in Section 4.2. Fig. 15 shows that the X- and Y-axis positions are fed back using linear encoders (MicroE 2000), which are decoded using blocks DS1104ENC_POS_C1 and DS1104ENC_POS_C2. The X- and Y-axis positioning error for the PI feedback control can then be obtained by comparing the positioning feedback signals from the desired input. The PI feedback control is combined with the feed-forward controls to produce the control signals, which are converted to analog signals by blocks DS1104DAC_C1 and DS1104DAC_C5 for the control voltages of the X- and Y-axes, respectively. The output signals are then amplified by the voltage amplifier (PA 45) to actuate the PAs so that the FBM tracks the desired trajectory. After describing the real-time Simulink code for the dSPACE system, a circular contouring task is designed to validate the proposed controller as Case study II.

Case II.

The contouring task used to validate the performance of the proposed method is

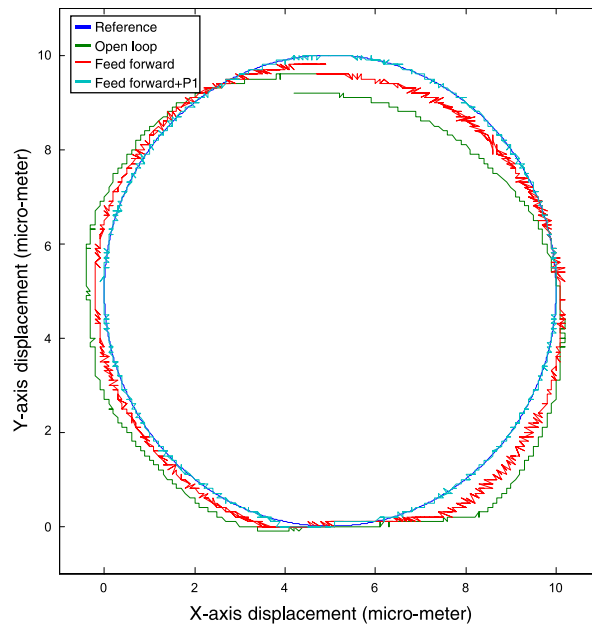
$$\begin{cases} x(t) = 5 + 5 \sin 2\pi t \text{ (}\mu\text{m)} \\ y(t) = 5 + 5 \cos 2\pi t \text{ (}\mu\text{m)}. \end{cases} \quad (57)$$

The feed-forward controller based on Bouc–Wen model combined with PI feedback controller is applied to the tracking task. The parameters for the PI feedback controller are $K_p = 0.8$ and $K_I = 480$ for each X-axis and Y-axis of FBM stage. Figs. 16 and 17 show the experimental results, which describe the contouring responses and contouring errors for the open-loop, feedforward controller, and feed-forward control with PI feedback controller. In this case, the frequency of reference is 1 Hz, and the experimental results show that the open loop has a maximal tracking error of $0.82 \mu\text{m}$. When the feedforward controller is applied, the maximal contouring error decreases to $0.35 \mu\text{m}$. When using the proposed feedforward control, however, some tracking errors result from modeling uncertainties and external disturbance. The precision of the PAFBM is

Table 9

The RMSE of the proposed method with biaxial actuated base on X- and Y-axis FBM.

RMSE Frequency	X-axis FBM tracking error (μm)		Y-axis FBM tracking error (μm)	
	1 Hz	5 Hz	1 Hz	5 Hz
Feed-forward	0.17041	0.15869	0.13978	0.09953
Feed-forward + PI	0.03849	0.07611	0.03432	0.07081

**Fig. 16.** The contouring responses for the PAFBM for the open loop, the feedforward and the feed-forward control combined with PI feedback controller.

improved by combining the proposed feed-forward control with PI feedback controller, which effectively compensates for modeling error and external disturbance. After using the PI feedback controller, contouring errors are limited to $0.1 \mu\text{m}$. The effects of the reference frequency are also analyzed. Table 9 shows the response for the proposed method with respect to the sinusoidal input at frequencies of 1 and 5 Hz. Although the reference input frequency increases from 1 to 5 Hz, the experimental results show that the proposed method can perform contouring tasks to within $0.1 \mu\text{m}$.

5. Conclusion

The proposed generalized Duhem model (GDM) for the piezo-electrical actuator's hysteresis model reformulates the Duhem model, Bouc–Wen model and Dahl model as a specified GDM for modeling the piezo-actuated stage. Based on GDM structure, Bouc–Wen and Dahl models are special cases of GDM, where the hysteresis force $F_h(t)$ depends only on $\dot{u}(t)$ and is independent of $\dot{x}(t)$ in the Bouc–Wen model whereas it depends only on $\dot{x}(t)$ and is independent of $\dot{u}(t)$ in the Dahl model. In the Duhem model, which includes both electrical and mechanical domains, the hysteresis force $F_h(t)$ depends on $\dot{x}(t)$ and $\dot{u}(t)$. To model the hysteresis nonlinear, the hysteresis dynamics must be established by GDM, and PSO is used to identify system parameters *via* the nonlinear optimization formulation. After optimizing the system parameters, the proposed feedforward compensation based on Duhem model with crossover terms effectively alleviates cross-coupling effects between the X- and Y-axis actuation. The effectiveness of the proposed model is verified in a real-time feedforward control implemented using the optimal parameters obtained by PSO. The proposed feed-forward control with PI feedback controller effectively compensates for nonlinearities in the tracking task when contouring errors are smaller than $0.1 \mu\text{m}$. Therefore, the real-time experimental results confirm that the proposed controller can perform tracking tasks with submicron precision.

Acknowledgments

The authors would like to thank the National Science Council of the Republic of China, Taiwan for financially supporting this research under Contract No. NSC 100-2221-E-027 -031. Ted Knoy is appreciated for his editorial assistance.

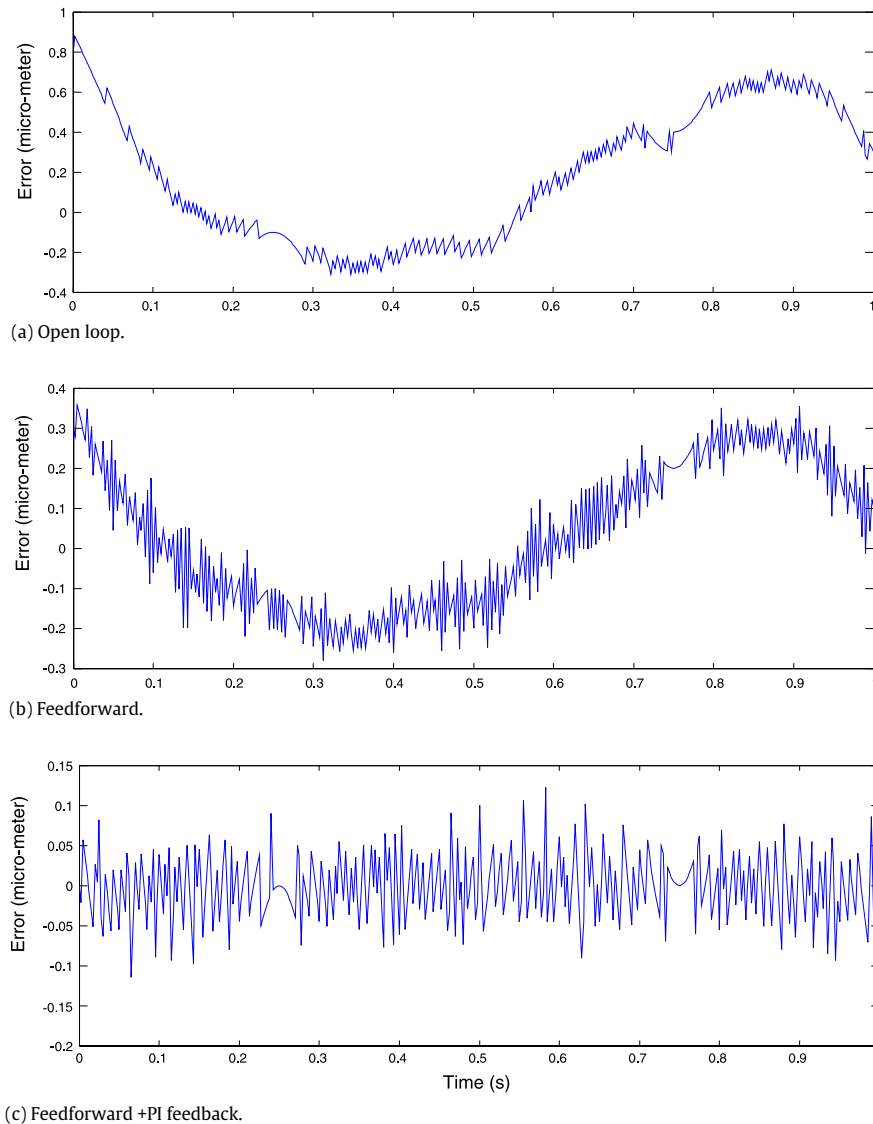


Fig. 17. The contouring errors for the PAFBM for (a) the open loop, (b) the feedforward controller and (c) the feed-forward control with PI feedback controller.

References

- [1] J.W. Macki, P. Nistri, P. Zecca, Mathematical models for hysteresis, *SIAM Rev.* 35 (1) (1993) 94–123.
- [2] M.A. Krasnosel'skii, A.V. Pokrovskii, *Systems with Hysteresis*, Springer-Verlag, New York, 1980.
- [3] I.D. Mayergoyz, Dynamic Preisach models of hysteresis, *IEEE Trans. Magn.* 24 (6) (1988) 2925–2927.
- [4] B.D. Coleman, M.L. Hodgdon, A constitutive relation for rate independent hysteresis in ferromagnetically soft materials, *Internat. J. Engrg. Sci.* 24 (1) (1986) 897–919.
- [5] Y.K. Wen, Method for random vibration of hysteresis systems, *J. Eng. Mech. Div.* 102 (2) (1976) 249–263.
- [6] J.L. Ha, Y.S. Kung, R.F. Fung, S.C. Hsien, A comparison of fitness functions for the identification of a piezoelectric hysteretic actuator based on the real-coded genetic algorithm, *Sensors Actuators A* 132 (1) (2006) 643–650.
- [7] C.J. Lin, S.Y. Chen, Evolutionary algorithm based feedforward control for contouring of a biaxial piezo-actuated stage, *Mechatronics* 19 (6) (2009) 829–839.
- [8] Q.S. Xu, Y.M. Li, Dahl model-based hysteresis compensation and precise positioning control of an XY parallel micromanipulator with piezoelectric actuation, *Trans. ASME J. Dyn. Syst. Meas. Control* 132 (2010) 041011–1–041011–12.
- [9] L.O. Chua, S.C. Bass, A generalized hysteresis model, *IEEE Trans. Circuit Theory* 19 (1972) 36–48.
- [10] J.V. Leite, N. Sadowski, P. Kuo-Peng, N.J. Batistela, J.P.A. Bastos, The inverse Jiles–Atherton model parameters identification, *IEEE Trans. Magn.* 39 (3) (2003) 1397–1400.
- [11] L.O. Chua, S.C. Bass, A generalized hysteresis model, *IEEE Trans. Circuit Theory* 19 (1) (1972) 36–48.
- [12] H. Zhang, T. Higuchi, N. Nishioki, Dual tunneling-unit scanning tunneling microscope for length measurement based on crystalline lattice, *J. Vac. Sci. Technol.* 2 (15) (1997) 174–177.
- [13] M.J. Jang, C.L. Chen, J.R. Lee, Modeling and control of a piezoelectric actuator driven system with asymmetric hysteresis, *J. Franklin Inst.* 346 (1) (2009) 17–32.

- [14] A.J. Fleming, High-speed vertical positioning for contact-mode atomic force microscopy, in: *Proc. IEEE/ASME Int. Conf. Adv. Intell. Mechatron.*, Singapore, 2009, pp. 522–527.
- [15] O.M.E. Rifai, K. Youcef-Toumi, Coupling in piezoelectric tube scanners used in scanning probe microscopes, in: *Proc. Amer. Control Conf.*, vol. 4, 2001, pp. 3251–3255.
- [16] J.W. Ryu, D.G. Gweon, K.S. Moon, Optimal design of a flexure hinge based XYZz wafer stage, *Precis. Eng.* 21 (1) (1997) 18–28.
- [17] S.H. Chang, K.T. Chung, C.C. Hon, An ultra-precision XYZz piezo-micropositioner part I: design and analysis, *IEEE Trans. Ultrason. Ferroelectr. Freq. Control* 46 (1) (1999) 897–905.
- [18] C.W. Lee, S.W. Kim, An ultraprecision stage for alignment of wafers in advance microlithography, *Precis. Eng.* 21 (1) (1997) 113–122.
- [19] K.K. Leang, A.J. Fleming, High-speed serial-kinematic AFM scanner: design and drive considerations, *Asian J. Control* 11 (2) (2009) 144–153.
- [20] G. Schitter, P.J. Thurner, P.K. Hansma, Design and input-shaping control of a novel scanner for high-speed atomic force microscopy, *Mechatronics* 18 (5–6) (2008) 282–288.
- [21] R.F. Fung, Y.L. Hsu, M.S. Huang, System identification of a dual-stage XY precision positioning table, *Precis. Eng.* 33 (1) (2009) 71–80.
- [22] J.H. Oh, D.S. Bernstein, Semilinear Duhem model for rate-independent and rate-dependent hysteresis, *IEEE Trans. Automat. Control* 50 (5) (2005) 631–645.
- [23] G.M. Clayton, S. Tien, K.K. Leang, Q. Zou, S. Devasia, A review of feedforward control approaches for nano precision positioning in high speed SPM operation, *Trans. ASME J. Dyn. Syst. Meas. Control* 131 (2009) 061101-1–061101-19.
- [24] M. Goldfarb, N. Celanovic, Modeling piezoelectric stack actuators for control of micromanipulation, *IEEE Control Syst. Mag.* 17 (1) (1997) 69–79.
- [25] H.J.M.T.S. Adriaens, W.L. De Koning, R. Banning, Modeling piezoelectric actuators, *IEEE/ASME Trans. Mechatronics* 5 (4) (2000) 331–341.
- [26] J. Kennedy, R.C. Eberhart, Particle swarm optimization, in: *Proceedings of the IEEE, International Conference on Neural Networks Perth, Australia*, 1995, pp. 1942–1948.
- [27] M. Clerc, J. Kennedy, The particle swarm-explosion, stability and convergence in a multidimensional complex space, *IEEE Trans. Evol. Comput.* 6 (1) (2002) 58–73.
- [28] K.K. Leang, Q. Zou, S. Devasia, Feedforward control of piezoactuators in atomic force microscope systems: inversion-based compensation for dynamics and hysteresis, *IEEE Control Syst. Mag.* 29 (1) (2009) 70–82.
- [29] J.G. Ziegler, N.B. Nichols, Optimum settings for automatic controllers, *Trans. ASME* 64 (1942) 759–768.
- [30] C.L. Chen, K.S. Li, Observer-based robust AILC for robotic system tracking problem, *J. Chin. Soc. Mech. Eng.* 30 (6) (2009) 483–491.
- [31] Yun-Ze Li, Chieh-Li Chen, Modeling and analysis of thermal-management impacts on transient performances of PEM fuel cells, *J. Chin. Soc. Mech. Eng.* 32 (1) (2011) 15–23.